Multi-view Wire Art

KAI-WEN HSIAO, National Tsing Hua University
JIA-BIN HUANG, Virginia Tech
HUNG-KUO CHU, National Tsing Hua University

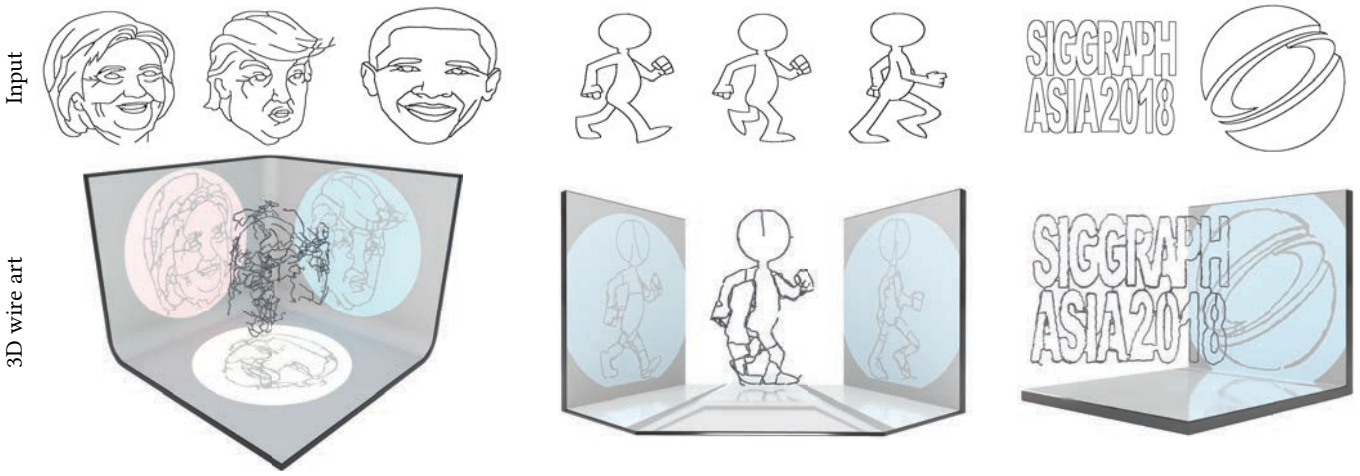

Fig. 1. We present an algorithm that takes line drawing images and the spatial arrangement of viewpoints as inputs and produces 3D wire sculpture art showing distinct interpretations when viewed at different angles. The generated 3D wire sculptures can be used to cast distinct shadows onto three mutually orthogonal planes (*left*), create different poses of an animated cartoon characters (*middle*), or exhibit two concepts at the same time, e.g., texts v.s. logo (*right*). The 3D wire art can be appreciated either with light sources casting shadows onto external planar surfaces or directly viewing from certain viewpoints.

Wire art is the creation of three-dimensional sculptural art using wire strands. As the 2D projection of a 3D wire sculpture forms line drawing patterns, it is possible to craft multi-view wire sculpture art — a static sculpture with multiple (potentially very different) interpretations when perceived at different viewpoints. Artists can effectively leverage this characteristic and produce compelling artistic effects. However, the creation of such multi-view wire sculpture is extremely time-consuming even by highly skilled artists. In this paper, we present a computational framework for automatic creation of multi-view 3D wire sculpture. Our system takes two or three user-specified line drawings and the associated viewpoints as inputs. We start with producing a sparse set of voxels via greedy selection approach such that their projections on the virtual cameras cover all the contour pixels of the input line drawings. The sparse set of voxels, however, do not necessary form one single connected component. We introduce a constrained 3D pathfinding algorithm to link isolated groups of voxels into a connected component while maintaining the similarity between the projected voxels and the line drawings. Using the reconstructed visual hull, we extract a curve skeleton and produce a collection of smooth 3D curves by fitting cubic splines and optimizing the curve deformation to best approximate the provided line drawings. We demonstrate the effectiveness of our system for creating compelling multi-view wire sculptures in both simulation and 3D physical printouts.

Authors' addresses: Kai-Wen Hsiao, National Tsing Hua University, kevin30112@gmail.com; Jia-Bin Huang, Virginia Tech, jbhuang@vt.edu; Hung-Kuo Chu, National Tsing Hua University, hkchu@cs.nthu.edu.tw.

CCS Concepts: • **Computing methodologies → 3D imaging**; **Parametric curve and surface models**;

Additional Key Words and Phrases: image-based modeling, wire art, skeleton extraction, shape deformation

ACM Reference Format:
Kai-Wen Hsiao, Jia-Bin Huang, and Hung-Kuo Chu. 2018. Multi-view Wire Art. *ACM Trans. Graph.* 37, 6, Article 242 (November 2018), 11 pages. https://doi.org/10.1145/3272127.3275070

1 INTRODUCTION

Wire sculpture is a unique art form that creates complex objects out of wire. The use of wire as a medium for sculpturing has been widely applied to furniture design [Postell 2012], crafting wire wrapped jewelry [Iarussi et al. 2015; WigJig 2015], and wire sculptural art [2007]. Very recently, French artist Matthieu Robert-Ortis has created compelling wire sculptures that exhibit two distinct image interpretations when viewed at different perspectives. Figure 2 presents two examples of *multi-view wire sculpture art.* [1]

Similar to shadow art, multi-view wire art allows us to create objects with multiple interpretable line drawings at different viewpoints. Furthermore, wire art offers additional flexibility in that the

[1]More examples can be found at http://cargocollective.com/matthieu-robert-ortis/En-video

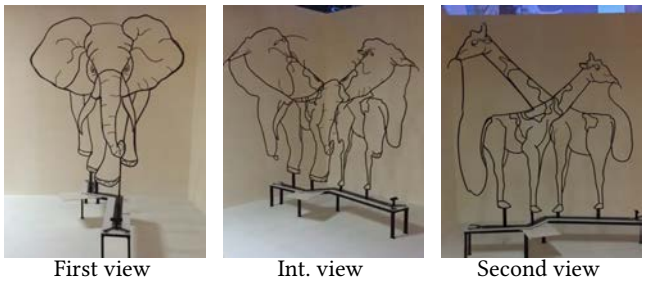

Fig. 2. **Example of multi-view wire sculpture art.** The anamorphose sculpture created by the French sculptor Matthieu Robert-Ortis is a classic example of *multi-view wire art*. When viewing from one specific angle, we perceive a drawing of an elephant. When viewing from another view point, the interpretation changes into two giraffes. The 2D projection in the intermediate view does not produce an interpretable image.

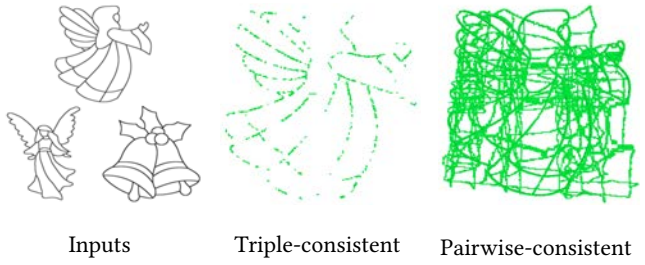

Fig. 3. **Conflicting silhouette constraints.** (*Left*) Three input line drawings. (*Middle*) When constructing the visual hulls using the three input silhouettes at mutually orthogonal viewpoints, selecting voxels by intersecting the generalized cones from all three views (i.e., triplet-consistent) only produces very sparse points at the projected view. (*Right*) Keeping voxels that are consistent with at least a pair of views (i.e., pairwise-consistent) helps increase the coverage of the desired line contour, but yield unrecognizable image due to conflicting constraints.

wire sculpture does not require a light source for casting shadows to see the hidden images. It is thus of great interests for enabling designers and hobbyists to create multi-view wire art. However, designing and creating multi-view wire art is prohibitively difficult for novice users due to the required artistic skills and significant efforts in resolving conflicting contour constraints from two or more line drawings.

Our work. We present a system for enabling users to create the desired multi-view wire art sculpture. As shown in Figure 1, our system takes two or three line drawing images and the associated viewpoints provided by the user as inputs and produce the 3D wire sculpture that forms the user-specified line drawings at different viewpoints. This problem is challenging because the wire structure satisfying all constraints by input line drawings often does not exist (see Figure 3). To tackle the challenge, we develop tools for constructing the sculpture by balancing the smoothness of the curves and the similarity between the specified line drawing and the projection at multiple viewpoints.

Specifically, our approach consists of two main stages: (1) visual hull reconstruction, (2) 3D curve skeleton extraction and deformation. In the first stage, we use a greedy selection approach to generate a collection of voxels covering all the contour pixels of the input line drawings and introduce a constrained 3D pathfinding algorithm to link the resulting isolated components into one single connected component that represents the final visual hull. Second, based on the reconstructed visual hull, we extract a 3D curve skeleton by exploiting a novel quality measurement that captures projection errors and structural complexity of the curve skeleton. We then fit individual skeleton lines using cubic splines and perform image-guided curve deformation to improve the projection error with respect to the input line drawings. Although our algorithm runs automatically, we provide interactive tools that enable interactive editing for users to repair or simplify the generated wire sculpture using 2D strokes. We demonstrate the effectiveness of our system on a wide variety of different line drawings. Numerous results show that the proposed method can produce multi-view wire sculptures with small distortions in the projected views.

Our contributions. (1) A system for the automatic creation of multi-view wire sculpture art using only user-specified 2D line drawings and the associated viewpoints. Our system is capable of generating complex wire sculptures that are extremely difficult to design and implement manually (e.g., three views); (2) A suite of computational techniques tailored to resolving conflicting constraints from multiple views while maintaining similarity between the projections and the input line drawings; (3) A characterization of quality over voxel resolution and the interval of viewing directions.

2 RELATED WORK

3D reconstruction. Our problem builds upon the concepts and techniques in 3D reconstruction from multiple 2D image observations. Structure-from-motion (SfM) [Schonberger and Frahm 2016; Snavely et al. 2006] and multi-view stereo (MVS) [Collins 1996; Furukawa and Ponce 2010; Goesele et al. 2007; Huang et al. 2018; Kuhn et al. 2017; Schönberger et al. 2016] algorithms are capable of reconstructing detailed 3D models in unconstrained settings (e.g., photos from the Internet). We refer the readers to [Furukawa and Hernández 2015] for a comprehensive overview of MVS algorithms. These methods, however, rely on establishing point correspondence across images and therefore have difficulty in handling smooth regions or thin wire structures. In light of this, several recent approaches exploit higher order features such as lines or curves as primitives for 3D reconstruction [Fabbri and Kimia 2010; Hofer et al. 2017; Liu et al. 2017; Usumezbas et al. 2016]. Assuming clean foreground-background separation, visual hull and silhouette intersection based algorithms can be also applied to construct 3D models from image observations [Laurentini 1994; Lazebnik et al. 2007; Matusik et al. 2000; Szeliski 1993] or from user-specified sketchs [Olsen et al. 2009; Rivers et al. 2010]. Similar to visual hull based algorithms, our method also uses multiple silhouettes (from user-specified line drawings) as inputs to construct a 3D model of a wire sculpture where its projections match with the input silhouettes as much as possible. The difference lies in that our input silhouettes may conflict with each other (see an example in Figure 3) and produce many isolated components in the visual hull, causing difficulty in manufacturing

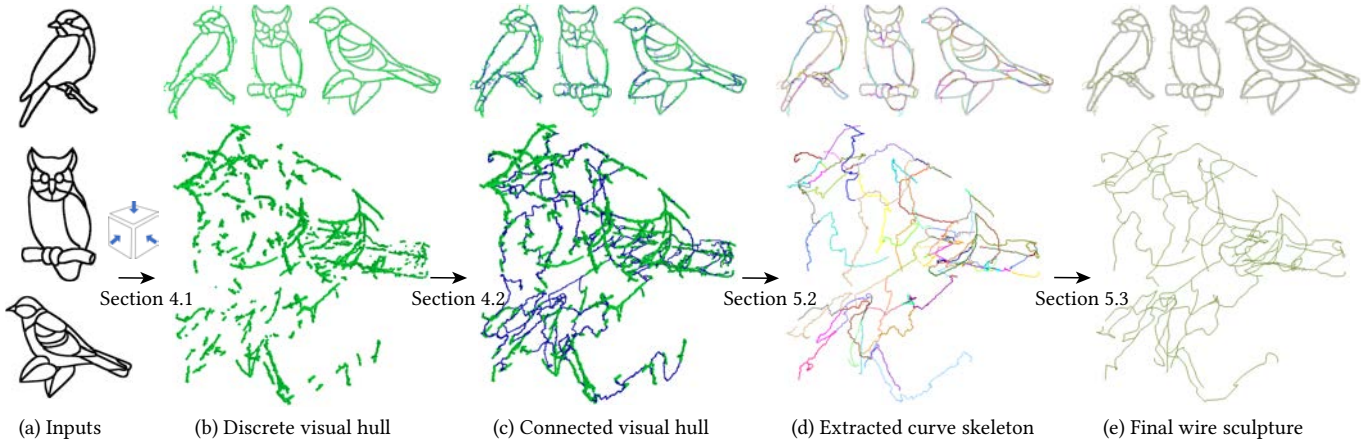

Fig. 4. **Method overview**. Given three input line drawing images (a), our system starts with reconstructing a discrete visual hull (b) through intersecting generalized cones formed by back-projecting the 2D image to 3D using the associated camera parameters (mutually orthogonal viewpoints in this example). We then integrate the isolated components (green voxels) into a connected visual hull (c) via a 3D pathfinding method that jointly analyzes the spatial relations between components in 3D and their 2D counterparts. The traced 3D pathes are represented by blue voxels. Next, we apply a volumetric thinning algorithm [Liu et al. 2010] to extract a curve skeleton from the reconstructed visual hull, followed by a structure simplification process that grounds a tailor-made quality measurement to strike a balance between i) the projection error and ii) the structure compactness of resulting curve skeleton (d). Lastly, we fit the individual skeleton lines (colored line segments) with cubic splines and employ an image-guided 3D curve deformation to obtain the final smooth, continuous, and compact 3D wire sculpture (e). (*Top* row) The projections of intermediate products using associated camera parameters.

a physical wire sculpture. Our work focuses on resolving the inconsistency and constructing a collection of smooth, continuous curve skeletons while minimizing the distortion between the projected views and the input line drawings.

Multiple interpretations from an object. Our work on creating multi-view wire art is related to several approaches for producing multiple visual interpretations from a single object. The perception of a *static* object (e.g., image, relief, sculpture) can vary dramatically depending on viewing distances [Oliva et al. 2006], figure-ground organization [Kuo et al. 2016], illumination from a certain direction [Alexa and Matusik 2010; Bermano et al. 2012], viewing directions [Keiren et al. 2009; Sela and Elber 2007], or casting shadows onto external planar surfaces [Min et al. 2017; Mitra and Pauly 2009]. Won and Lee [2016] further extended the idea to create shadow theatre from *dynamic* objects (i.e., animated characters). Our work differs in that we use 3D wire as a medium, allowing us to exhibit a clear prescribed line drawing either from certain viewing directions or cast shadows on planar surfaces using a point light source.

Wire sculpture design and modeling. More recently, there is a line of works devoted to modeling and fabricating the wire sculptures of a specific form. Iarussi *et al.* [2015] presented a computational framework to assist the creation of wire wrapped jewelry. Liu *et al.* [2017] extended the dimension from 2D to 3D modeling of wire sculptures using only a few input images of physical objects. Miguel *et al.* [2016] proposed a computer-aided tool to facilitate converting a 3D model into a stable, self-supporting wire sculpture that is fabricatable with a 2D wire bending machine. Similarly, Zehnder *et al.* [2016] developed a computational design tool, targeting for the fabrication of ornamental curve networks defined on the 3D surfaces. Our work also falls into the category of 3D wire design and modeling but targets fundamentally different context.

3 METHOD OVERVIEW

Our system takes input as a set of 2D line drawing images (or simply images), $\mathcal{I} = \{I_1, ..., I_n\}$, along with the associated camera parameters specified by an user (i.e., pose, and perspective or orthogonal projection), $\mathcal{P} = \{P_1, ..., P_n\}$, where $n = \{2, 3\}$ views in our experiments. Our goal is to reconstruct a set of 3D curves $C = \{C_1, ..., C_k\}$ represented by cubic splines. These curves together form a smooth, continuous, and compact 3D wire sculpture, which while seemingly irregular in both its geometry and structure, can precisely interpret the input images when viewed or cast shadows from the specified viewpoints. Figure 4 presents an overview of our system.

Pre-processing. For each input image, I_k, we first apply a simple thresholding and thinning algorithm to extract a set of one-pixel wide 2D curve lines. We represent these foreground pixels of I_k as a graph $G_k = \{V_k, E_k\}$, where V_k are pixels along the curve lines and E_k encode their connectivities. If the graph G_k contains multiple connected components, we further add edges to connect them according to their spatial proximity and use a conventional minimum spanning tree algorithm to get a connected graph.

Given the preprocessed input images, our system starts by back-projecting the foreground pixels to the 3D domain using the associated camera parameters to form a set of generalized cones [Laurentini 1994]. We then discretize the space into volumetric grids (or voxels) and find a minimum set of voxels such that the foreground pixels in each view can be completely covered by the projections of voxels. Applying a flooding algorithm produces a *discrete visual hull*, which often contains an excessive amount of isolated components in our context (Figure 4(b), Section 4.1). To integrate these isolated

components into one connected component, we first connect two proximate components via a 3D pathfinding method that jointly analyzes the spatial relations between two components in 3D and their 2D counterparts. Then we solve a binary labeling problem that retains necessary links to form a *connected visual hull* while minimizing the projection error due to the additional inconsistent voxels from the links (Figure 4(c), Section 4.2).

Here, the reconstructed visual hull represents a well-defined space in 3D where the curves of final wire sculpture would lie in. We first adopt a state-of-the-art volumetric thinning algorithm [Liu et al. 2010] to effectively compute a shape- and topology-preserving curve skeleton from the reconstructed visual hull. However, the extracted curve skeleton is typically complex in geometry, contains numerous redundant parts, and thus requires further refinement to be physically realizable (e.g., 3D printing). To this end, we devise a novel quality measurement tailored for wire modeling (Section 5.1) by iteratively removing the constituent skeleton lines to strike a balance between projection error and structure compactness (Figure 4(d), Section 5.2). Finally, we obtain a smooth, continuous, and compact 3D wire sculpture by fitting individual skeleton lines with parametric cubic splines, followed by an image-guided curve deformation to improve the projection accuracy with respect to the input images (Figure 4(e), Section 5.3).

4 VISUAL HULL RECONSTRUCTION

Reconstructing a 3D wire sculpture from multiple reference 2D images is related to shadow art [Mitra and Pauly 2009] as well as shape-from-silhouette applications [Laurentini 1994]. In this section, we describe a common step shared by existing works to reconstruct a 3D *visual hull* — a set of voxels whose projections best approximate the reference images using the associated camera parameters. With the reconstructed visual hull, we can then extract a compact wire sculpture with smooth, continuous 3D curves. Specifically, we aim to reconstruct the visual hull meeting the following two requirements: (1) *Completeness*: all the foreground pixels in the reference line drawings should be covered by the projections of the visual hull (Section 4.1); (2) *Connectivity*: the constituent voxels of the visual hull must form a connected component (Section 4.2).

4.1 Discrete Visual Hull Generation

Given a set of *reference images*, denoted as $\{G_k, P_k | k = 1 \sim n\}$, our system starts by back-projecting the 2D image, $G_k = \{V_k, E_k\}$, to 3D using the camera projection parameters, P_k, and generating a set of generalized cones. To find a 3D volume that is compatible with G_k and P_k, we compute a bounding cube based on the intersection of camera's viewing frustums. We then discretize the cubic volume into $N \times N \times N$ uniform voxels $x_i \in \mathbb{R}^3$ with N indicates the resolution of voxelization. We define the relations between voxels and the reference images as follows. Let $\tilde{x}_i^k \in \mathbb{R}^2$ be the 2D projection of i$^{\text{th}}$ voxel x_i with respect to projection P_k for the k^{th} view. We label a image pixel $\mathbf{p}^k \in V_k$ as *complete* if it falls within one of the circles (with a radius of 2 pixels) centered at $\tilde{x}_i^k$. We call a voxel *consistent* if it can establish the mapping $(\tilde{x}_i^k, V_k)$ for all k views.

The reconstruction process starts by initializing the visual hull with a set of *consistent* voxels. Not surprisingly, the projection of these voxels leads to highly incomplete images due to the inconsistency between the reference images (Figure 5(left)). Mitra and Pauly [2009] tackle the inconsistency problem by a global optimization that deforms the reference images. While such a deformation framework performs well for solid shapes, it becomes ill-posed for line drawing images that contain many hollow regions formed by thin and complex line structures. We propose a simple yet effective approach to further expand visual hull with voxels that are aware of both i) projection error in 2D and ii) spatial compactness in 3D. For each of the incomplete pixel $\mathbf{p}^k \in V_k$, we can find a ray of voxels that map to $\mathbf{p}^k$. To favor voxels that have small projection errors and are spatially close to the target visual hull, we define the cost of the i$^{\text{th}}$ voxel x_i as follows:

$$\sum_{k=1}^{n} D_k(\tilde{x}_i^k) + (1 - \sum_{x_j \in N_{x_i}} D_{\text{prox}}(x_i, x_j)), \tag{1}$$

where D_k is a distance transform map that measures the projection error with respect to image G_k. The term N_{x_i} contains the voxels in the visual hull as well as $12 \times 12 \times 12$ neighboring voxels to x_i. The function $D_{\text{prox}}(x_i, x_j)$ computes the proximity between voxels using a normalized Gaussian kernel with $\mu = x_i$ and $\sigma = 2$. Then, we employ a greedy algorithm that expands the visual hull by selecting the least-cost voxel for each incomplete pixel $\mathbf{p}^k$ and repeats the process until all the pixels in V_k are labeled as *complete*. As shown in Figure 5(right), this process results in a *discrete visual hull* that fulfills the completeness requirement. We include the pseudocode that details the above procedure in the supplementary document.

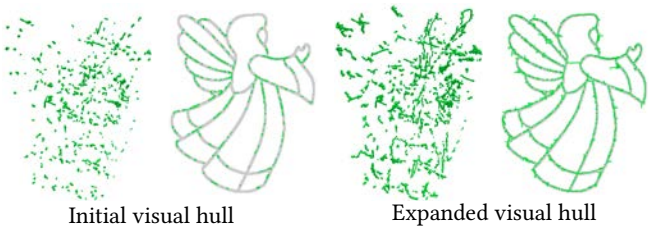

Fig. 5. **Initial vs. expanded visual hull**. Given the same inputs as in Figure 3, (*Left*) the initial visual hull with only triple-consistent voxels produces sparse structure and incomplete projection. (*Right*) Exanding the initial visual hull with voxels that are aware of both i) projection error and ii) spatial compactness leads to a projection covering complete image contours without introducing severe artifacts.

4.2 Connectivity Optimization

The discrete visual hull typically contains an excessive amount of isolated components. These isolated components significantly increase the difficulty in manufacturing a physical wire sculpture. Therefore, our goal in this step is to find an optimal set of 3D paths such that the isolated components are linked to form a *single connected component* while minimizing the projection error caused by inconsistent voxels that compose the 3D paths. We formulate the problem as a conventional minimum spanning tree problem on a graph representing the isolated components and their spatial relationships.

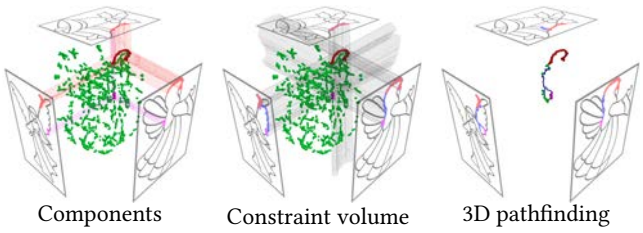

Fig. 6. **Constrained 3D pathfinding**. (*Left*) Given two components in 3D (red and purple voxels), we first find their 2D conterparts in each view. (*Middle*) We then back-project the 2D shortest paths along the line contours in the projected views (blue pixels) and construct a constraint volume by taking the union of the generalized cones. (*Right*) 3D pathfinding algorithm traces a sequence of voxels (blue voxels) to connect the two components.

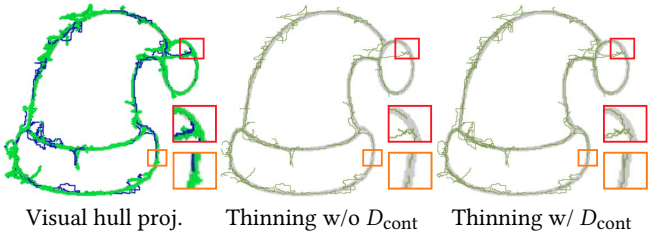

Fig. 7. **Continuity penalty.** (*Left*) Projection from the reconstructed visual hull. (*middle*) Applying volumetric thinning algorithm on the visual hull may result in broken line segments. (*Right*) Incorporate the continuity panelty D_{cont} in the edge weights w_{ij} help alleviate endpoints shrinkage artifacts.

Graph construction. First, we apply a flooding algorithm to constituent voxels of discrete visual hull and generate a collection of isolated components, denoted as $\mathcal{X} = \{X_1, ..., X_m\}$. Next, we construct a *component graph* $\mathcal{G} = \{\mathcal{X}, \mathcal{E}\}$ by adding a graph edge e_{ij} to $\mathcal{E}$ if the shortest distance between two components X_i and X_j is below a pre-defined threshold (15% of the edge length of the bounding cube in our experiments). For each graph edge e_{ij}, we employ the A^* pathfinding algorithm with best-first-search strategy to trace a 3D path from X_i to X_j. Two voxels, $x_{\text{src}} \in X_i$ and $x_{\text{dst}} \in X_j$, which define the shortest distance between X_i and X_j, represent respectively the source and destination for 3D pathfinding. We define a heuristic function for guiding pathfinding as follows:

$$h(x_i) = \sum_{k=1}^{n} D_k(\tilde{x}_i^k) + 0.6\|x_i - x_{\text{dst}}\|_2^2. \tag{2}$$

The first term encourages selecting a voxel with smallest projection error, while the second term regularizes the tracing direction toward the destination voxel x_{dst}. The resulting 3D path, composed of voxels that connect the two components X_i and X_j, is denoted as $\mathcal{P}_{ij}$.

Constrained 3D pathfinding. Note that a greedy pathfinding algorithm that freely explores the volume space is computationally expensive. Here, we exploit the mapping between the target visual hull and the input images to construct a volumetric manifold to which the searching space is restrained while maintaining the projection quality. Specifically, given a pair of components $\{X_i, X_j\}$ and corresponding projections $\{\tilde{X}_i^k, \tilde{X}_j^k\}$ by P_k, we compute a 2D shortest path from $\tilde{X}_i^k$ to $\tilde{X}_j^k$ on the k-th input image G_k, and back-project pixels in the shortest path to obtain a constraint volume, denoted as $H_{i,j}^k$. We define the constraint volume as $H_{i,j} = \bigcup_{k=1\sim n} H_{i,j}^k$, where n is the number of input images. Intuitively, as the constraint volume $H_{i,j}^k$ has projections along the contour on k^{th} image, tracing path within the constraint volume thus does not incur additional projection errors while pruning out a large portion of the volume space. We modify the pathfinding algorithm to consider only voxels in $H_{i,j}$ when connecting components X_i and X_j and hence obtain a significant boost in timing (Section 7.2). Figure 6 illustrates the proposed constrained 3D pathfinding approach.

Shape-aware edge weight. We define the edge weight w_{ij} in the component graph as follows:

$$w_{ij} = \frac{1}{|\mathcal{P}_{ij}|} \sum_{\forall x_i \in \mathcal{P}_{ij}} \sum_{k=1}^{n} D_k(\tilde{x}_i^k) + D_{\text{cont}}(X_i, X_j). \tag{3}$$

Intuitively, the first term measures the projection error induced from path $\mathcal{P}_{ij}$ with respect to the input images. Here, we introduce the *continuity penalty* term, $D_{\text{cont}}(X_i, X_j)$, to avoid endpoints shrinkage effects due to volumetric thinning as follows:

$$D_{\text{cont}}(X_i, X_j) = \begin{cases} 0, & \exists k, \text{s.t. } \tilde{X}_i^k \cap \tilde{X}_i^k \neq \emptyset \\ 10, & \text{otherwise} \end{cases}, \tag{4}$$

$D_{\text{cont}}(X_i, X_j)$ captures whether the 2D projections of two disjoint components X_i and X_j form a continuous line segment in the projective views. If so, we want to ensure a path connecting two such components. This is achieved by adding a large constant value (10 in Equation 4) to those components that do not present such a relationship. Figure 7 shows the effect of this penalty term.

Optimization. We apply Kruskal's algorithm to the component graph $\mathcal{G}$ and obtain a minimum weight spanning tree. The final visual hull corresponds to the voxels that compose the resulting spanning tree.

5 3D CURVE EXTRACTION

In this section, we describe our method for extracting smooth and continuous 3D curves from the reconstructed visual hull. To this end, we first employ a volumetric thinning method [Liu et al. 2010] to extract a shape- and topology-preserving curve skeleton from the visual hull. This curve skeleton is then divided into a set of skeleton lines according to its topology. However, as the process of visual hull reconstruction is performed locally and does not take into account the compactness of global structure, the extracted curve skeletons may contain many redundant parts with complex geometry. This makes the physical realization process (e.g., 3D printing) extremely challenging, or not even possible. To tackle this problem, we perform a structure simplification on the curve skeleton that grounds on a novel quality measurement tailor-made for our context to strike a balance between projection error and structure compactness.

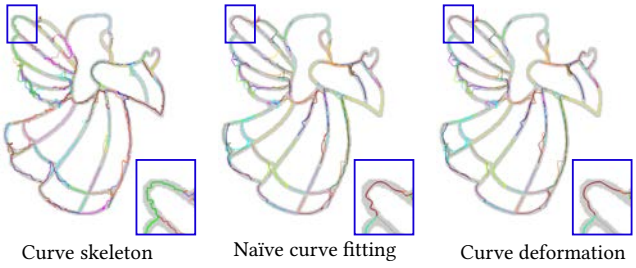

Fig. 8. **Effect of image-guided 3D curve deformation**. Given the extracted curve skeleton (*left*), using Naïve curve fitting may produce parametric curves that do not respect the given contours at the projected views (*middle*). The proposed image-guided 3D curve deformation step help reduce the distortion (*right*).

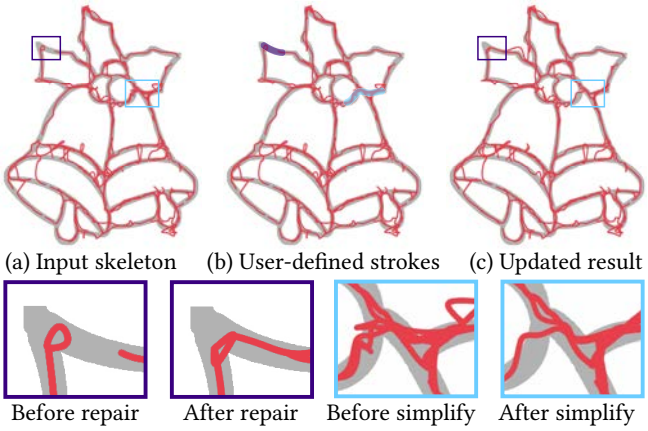

Fig. 9. **User editing example**. (a) The automatic structure simplification step may produce over-simplified skeleton (purple box) and under-simplified (light blue box) result. (b) The user can locally alter the result by specifying either *repair strokes* or *simplify strokes* on a particular input shape. (c) Given the user inputs, our system automatically updates the structure of associated skeleton lines to obtain a new result that respects user's intention at interative rate (see supplementary material for examples).

5.1 Quality Measurement

Given a curve skeleton denoted as $\mathcal{L} = \{L_1, ..., L_m\}$, where L_i represents the skeleton line that is composed of a sequence of skeleton points in 3D. We propose to measure the quality of $\mathcal{L}$ as:

$$E_{\text{quality}}(\mathcal{L}) = E_{\text{proj}}(\mathcal{L}) + \alpha E_{\text{struct}}(\mathcal{L}), \tag{5}$$

where E_{proj} and E_{struct} measure the *bidirectional projection error* and *structure compactness* of $\mathcal{L}$, respectively and the parameter α is used to control the relative weights between the two energy terms.

Bidirectional projection error. The bidirectional projection error aims to measure the shape similarity between the curve skeleton and input image in the projected view. Specifically, we propose to estimate (i) the *deviation*, indicating how much the projection of curve skeleton deviates from the input image; and (ii) the *incompleteness*, indicating how much portion of the input image is not recovered by the projection of curve skeleton. Note that we render the skeleton lines on the projected view using a circle shape with radius of 1 pixel width. We denote the foreground pixels of input image as V_k and projection of curve skeleton as $\tilde{\mathcal{L}}_k$. The projection error E_{proj} is of the form:

$$E_{\text{proj}}(\mathcal{L}) = \sum_{k=1}^{n} E_{\text{dev}}(\tilde{\mathcal{L}}_k, V_k) + w_k E_{\text{incomp}}(\tilde{\mathcal{L}}_k, V_k), \tag{6}$$

with

$$E_{\text{dev}}(\tilde{\mathcal{L}}_k, V_k) = \frac{1}{|\tilde{\mathcal{L}}_k|} \sum_{\forall \mathbf{p}^k \in \tilde{\mathcal{L}}_k} D_k(\mathbf{p}^k), \tag{7}$$

and

$$E_{\text{incomp}}(\tilde{\mathcal{L}}_k, V_k) = \frac{1}{|V_k|} \sum_{\forall \mathbf{p}^k \in V_k} D_{\tilde{\mathcal{L}}_k}(\mathbf{p}^k). \tag{8}$$

Two functions, D_k and $D_{\tilde{\mathcal{L}}_k}$, represent the distance transform maps computed by input V_k and the projected image $\tilde{\mathcal{L}}_k$, respectively. The parameter w_k controls the relative importance between energy functions with respect to each input image, and can be utilized to support flexible user controls (Section 6).

Structure compactness. The structure compactness energy term, on the other hand, aims to capture the complexity of curve skeleton in terms of its 3D structure and 2D counterparts in the projected views. We define the energy function as:

$$E_{\text{struct}}(\mathcal{L}) = E_{\text{redundancy}}(\mathcal{L}) + \beta E_{\text{complexity}}(\mathcal{L}). \tag{9}$$

The first term $E_{\text{redundancy}}$ measures the redundancy of mapping from curve skeleton to input images by counting how many points on the skeleton line $L_i \in \mathcal{L}$ map to the same foreground pixel $\mathbf{p}^k \in V_k$. The second energy function $E_{\text{complex}}(\mathcal{L})$ counts the number of skeleton lines in $\mathcal{L}$. The parameter β is used to trade off two energy functions. We empirically set $\alpha = 0.4$, $\beta = 0.38$, $w_k = 2$ in all experiments.

5.2 Curve Structure Simplification.

Given the definition of quality measurement on the curve skeleton, our goal here is to determine a subset of skeleton lines $\mathcal{L}' \subset \mathcal{L}$ so that we can minimize $E_{\text{quality}}(\mathcal{L}')$ while maintaining connectivity of the selected subset $\mathcal{L}'$. This amounts to a binary labeling problem over a set of skeleton lines, and thus existing global optimization methods are intractable. We implement a greedy approach to achieve approximate local minimum by iteratively removing skeleton lines using a priority queue. We leave the implementation details in the supplementary document.

5.3 3D Curve Fitting and Deformation

Given the curve skeleton, we can easily obtain a smooth and continuous wire sculpture by fitting the individual skeleton lines with parametric curve using cubic splines. However, a naïve curve fitting often leads to irregular curve shapes inherited from the zigzag features of reference skeleton lines (see Figure 8 (left, middle)). To avoid these artifacts, we devise a curve deformation model that iteratively

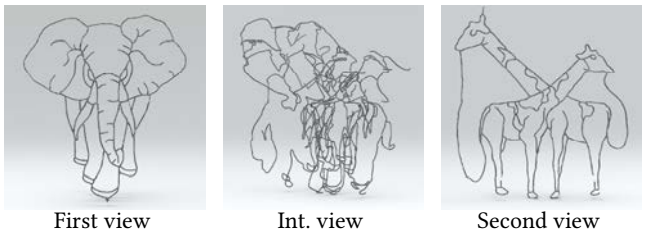

Fig. 10. **Reproducing artist's results.** Using artist's input of elephant/giraffe in Figure 2, our results show visually similar 2D projections as the input at both viewpoints. The intermediate view, however, reveals that our 3D wire sculpture has more complex structure than that from the artist (see Figure 2).

moves the control points on the curves toward the directions guided by the spatial relations between projected control points and input images. We show the effect of curve deformation in Figure 8 and refer the readers to the supplementary material for details.

6 USER CONTROL

While our method can produce a 3D wire sculpture that best approximates the given line drawings at the specified view in fully automatic fashion, the users may want to modify and refine the sculpture to enhance artistic effects of the structure or fix errors produced by our system. Here, we introduce two types of 2D strokes: (i) *repair strokes* and (ii) *simplify strokes* to support interactive user editing on the wire sculpture. The user simply needs to specify 2D strokes on the image of the wire sculpture projected onto the k-th input image, while our system will automatically update the local structure by (i) collecting skeleton lines that intersect with user strokes in the projected view; and (ii) re-running the structure simplification process on the selected skeleton lines with updated parameters. For the repair strokes, we increase the parameter w_k in Equation 6 from 2 to 8 to encourage the completeness in the k-th input image. For the simplify strokes, we double the parameter α in Equation 5 to amplify the structure compactness during the simplification. We demonstrate the effect of user editing in Figure 9.

7 EXPERIMENTAL RESULTS

7.1 Visual results

We evaluate our method on a wide variety of input line drawing images with varying complexity. We implement two types of exhibition modes: (i) orthogonal mode and (ii) in-plane mode. The former one arranges the virtual cameras in a mutually orthogonal setting, while the latter places all the cameras on the same plane with varying viewing angles. We automatically generated 20 multi-view wire sculptures in total. Figure 12 shows a gallery of the generated wire sculptures exhibited in orthogonal mode. Examples of in-plane exhibition mode can be found in Figure 1 (middle, right). In addition to static exhibition, the best way to demonstrate such a unique sculpture art is through a dynamic setting, where the 3D model, camera poses, and lighting are animated and working together to depict different input images over time. Please refer to supplementary material for more static and dynamic examples.

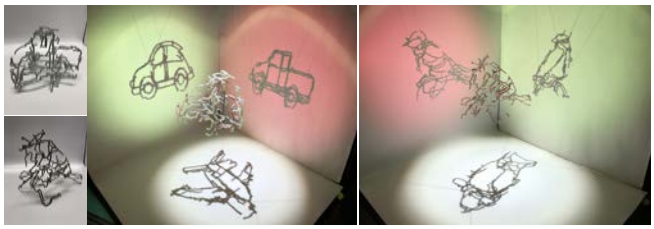

Fig. 11. **3D printouts.** Two 3D printouts of multi-view wire sculptures generated by our system using FDM (*middle*) and SLM (*right*) process.

Reproducing artist's results. We apply our method to reproduce the elephant/giraffe example. As shown in Figure 10, our 3D wire sculpture is as accurate as artwork in the projective views, but has slightly more complex structure than that by the artist (see Figure 2). Augmenting the inputs to three views (see Figure 12, 1st row) further demonstrates that our system can produce 3D wire sculptures that go beyond the complexity of existing pieces of art.

3D printout. To evaluate the physical realizability of the resulting 3D wire sculptures, we take two examples from our gallery and print out the models using industry-level 3D printing machines with different levels of resolutions. Specifically, the 3-transportation sculpture (Figure 12) was printed by a machine with 100-micron accuracy using FDM (fused deposition modeling) technique with PLA (polylactic acid). The 3-bird sculpture (Figure 4) was printed by a machine with 30-micron accuracy using SLM (selective laser melting) technique with metallic powders (CoCrMo alloy). Figure 11 shows the 3D printouts along with their physical exhibition. Note that the 3D printout may inevitably suffer from distortion due to the thin and curve shape of wire structure, and hence introduce more projection errors than its digital version.

7.2 Evaluation

In this section, we evaluate and characterize the performance of our method over several important design choices. The source code, input line drawings, and pre-computed wire sculptures will be made publicly available to stimulate further research.

Dataset and evaluation metrics. In addition to the triple-image examples shown in the paper, where the input images are from the same category and have similar complexity and style, we further prepared an extra set of 21 triple-image cases by randomly picking three images out of a large set of 45 input line drawing images with different styles and varying complexity.

We use two quantitative metrics to evaluate the quality of generated 3D wire sculptures. Our first metric measures the projection errors: $E_{\text{dev}} + E_{incomp}$ (Section 5.1). The project errors, however, may not reflect the quality well due to its sensitivity to outliers. Our second metric measures the projection accuracy by mean average precision (mAP). Specifically, we vary the distance threshold ranging from 0 (precise matching) to 10 pixels (coarse matching), compute the precision and recall at each step, and compute the mAP value across all images.

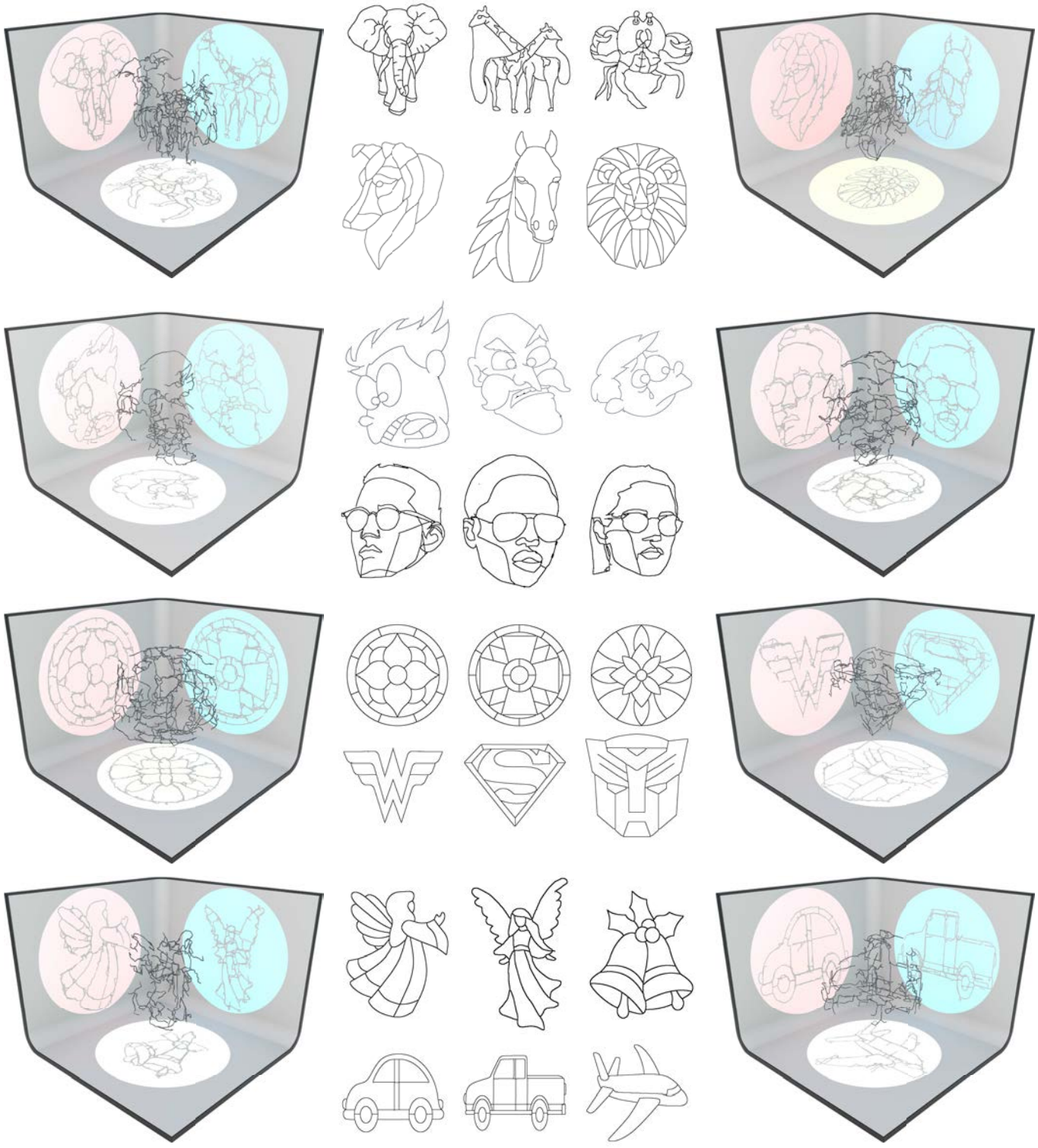

Fig. 12. **Visual results of multi-view wire art**. We present several examples of input line drawings with varying complexity. Given a set of three input images (*middle*), our system automatically generates 3D wires that exhibits three distinct line drawings when perceived from three orthogonal view points (*left*, *right*). Our method handles inputs with varying complexity. More results can be found in the supplementary material.

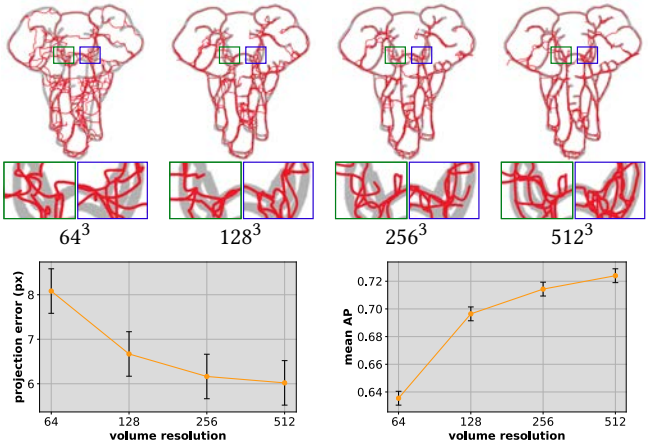

(a) Projection error (b) Mean average precision

Fig. 13. **Effect of voxelization resolution**. (*Top*) Increasing voxel resolution helps resolve the intricate details of the inputs in the projected images. (*Bottom*) Quantitative results in terms of (a) bidirectional projection error and (b) mean average precision. The error bars indicate the standard deviation computed from the set of examples in the dataset.

Resolution of voxelization. As the initial geometry and structure of 3D curve skeleton are determined by the reconstructed visual hull, voxel resolution plays a critical role in recovering the details of the visual hull, particularly due to the intricate details presented in the line drawings. We characterize the performance over voxel resolutions $N^3 = [512^3, 256^3, 128^3, 64^3]$ in orthogonal mode. Figure 13 shows a visual example as well as the quantitative results. Our results validate the intuition that increasing voxel resolution allows us to capture finer details in the inputs. However, this comes at the cost of memory and computational complexity. We believe that using an octree-based method can better address the trade-off than the uniform voxelization in this work.

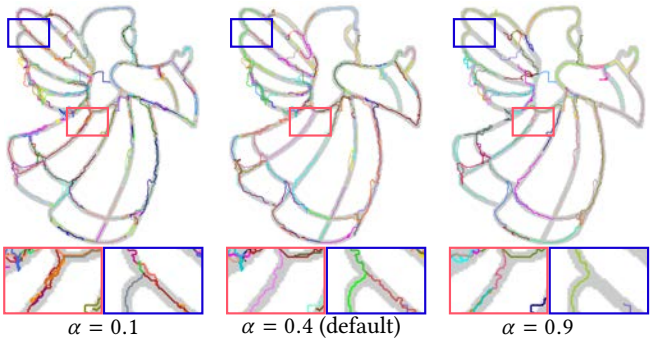

Fig. 14. **Trade-off between structure compactness and projection error.** Setting parameter α in Equation 5 to a small value (*left*) encourages extracting curves that align the line drawings well, but suffers from complex wire structure. On the other hand, setting a large value of α (*right*) produce simple wire structures with missing contour at projected views. We empirically set $\alpha = 0.4$ (fixed for all the experiments shown in the paper) to strike a balance between projection error and structure compactness.

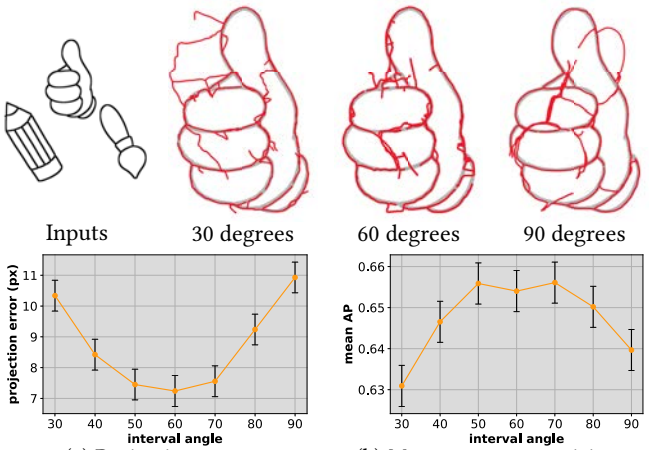

(a) Projection error (b) Mean average precision

Fig. 15. **Effect of angle intervals**. When placing all the three view points on the same plane, the reprojection accuracy depends heavily on the selected angle intervals. The similarity between the respective projections and the input images degrades significantly when angle intervals are small (because it is difficult to optimize the 3D wire with dramatically different projections under a small view point shift) or close to 90 degrees (because the first and the third views will be located at opposite viewing directions and create conflicting contours).

Effect of parameter α. In Section 5.1, we use a parameter α to control the relative importance between the projection error and structure compactness during the structure simplification process. Figure 14 shows the effect of α by generating curve skeleton with varying α. Setting α to either small value (0.1) or large value (0.9) may produce over-complex or over-simplified results. Our default setting with $\alpha = 0.4$ (fixed throughout all of our experiments) strikes a balance between projection error and structure compactness.

Viewing angles. In the in-plane mode with three images, we investigate the effect of angle interval and report the evaluation results in Figure 15. In the case of three input drawings, placing the viewpoints at an angle interval of 60 degrees achieves the best visual and quantitative results.

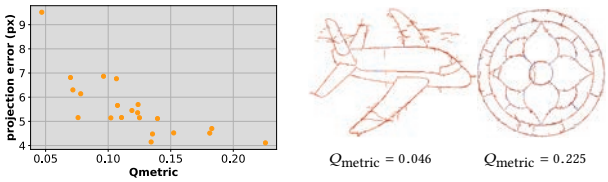

Fig. 16. **Quality indicator.** (*Left*) Scatter plot for the 21 cases. (*Right*) Two examples of lowest and highest value of Q_{metric}. The voxels of initial visual hull and expanded visual hull are colored in blue and red, respectively. Our quality indicator correlates well with the final projection errors of the wire sculptures.

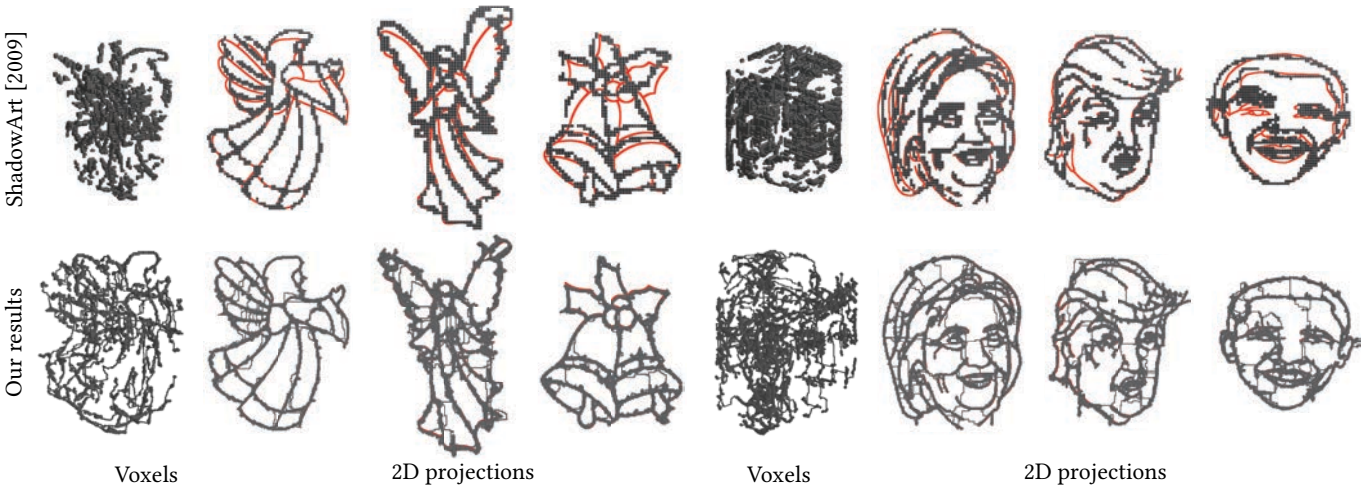

Fig. 17. **Comparision with Shadow Art.** (*Top*) The results of Shadow Art [Mitra and Pauly 2009] using input images from Figure 12 (7th row) and Figure 1 (left). (*Bottom*) The generated visual hull from our method using the same input images. The results from Shadow Art suffer numerous disjoint components in the reconstructed voxel structures and severely distored 2D projections that deviate from input line drawings (highlighted in red) due to image deformation.

Quality indicator. To evaluate how well the quality of the wire sculpture relates to the initial discrete visual hull, we propose a quality indicator metric, $Q_{\text{metric}} = |VH_{\text{initial}}|/|VH_{\text{expanded}}|$, which computes the ratio between the number of voxels in the initial visual hull VH_{initial} and that in the expanded visual hull VH_{expanded} (see Figure 5). Higher values of Q_{metric} indicate more triple-consistent voxels in the initial visual hull. For the 21 test cases used for evaluation, we found that the ratio correlates well with the projection errors with a Spearman's rank correlation coefficient = -0.818. Figure 16 shows the scatter plot of all 21 test cases. As computing the ratio Q_{metric} is efficient (< 1 minute), we can use it as quick test for quality, which allows us to filter out challenging cases that may lead to failures.

Timing analysis. Here we report the timing statistics of running our non-optimized method on the dataset using a moderate PC with an Intel Core i7 6700K (3.4GHz) and 32GB memory. The overall time complexity depends on the voxel resolution and the complexity of input images. For example, the average running time for simple images (e.g., 3rd row in Figure 12) and complex images (e.g., 1st row in Figure 12) with resolution 512^3 are 83 and 510 minutes, respectively. Decreasing the resolution to 256^3 will yield a 7X speedup. The major computational bottleneck lies in the connectivity optimization step in Section 4.2 (73% of the total running time). Using the proposed constrained 3D pathfinding algorithm provides more than 2X speedup. The structure simplification (Section 5.2) that occupies 27% of running time mainly depends on the complexity of input images. The average running time for generating discrete visual hull (Section 4.1) and curve fitting and deformation (Section 5.3) took about $1-3$ seconds and is thus negligible. Employing a hierarchical multi-scale implementation and parallelizing the sequential algorithm of 3D pathfinding can further speed up the system.

Comparision with Shadow Art. We ran the code of [Mitra and Pauly 2009] on 11 three-view examples. As shown in Figure 17, the resultant voxel structures generated by [Mitra and Pauly 2009] may contain many disjoint components due to the highly inconsistent nature of input line drawings. Moreover, a severely distorted projection is often inevitable due to an image deformation approach for eliminating inconsistent voxels. Our system, in contrast, can generate voxel structures with one single connected component without introducing significant projection errors. Please refer to the supplementary material for a complete set of comparison.

7.3 Limitations

Our method has limitations in the following aspects.

Results. Surprisingly, we find that the our method does not perform well on *simple* input images. Figure 18 shows an example in orthogonal mode. In this case, our method produces clearly visible artifacts due to the difficulty in resolving inconsistency from simple contours. Our approach also has difficulty in resolving dense line strokes (e.g., hairs) in the projected image due to limited voxel resolution.

Speed. Our current implementation may take up to several hours to construct a multi-view wire sculpture (depending on the chosen voxel resolution and input line drawing complexity). Once the initial

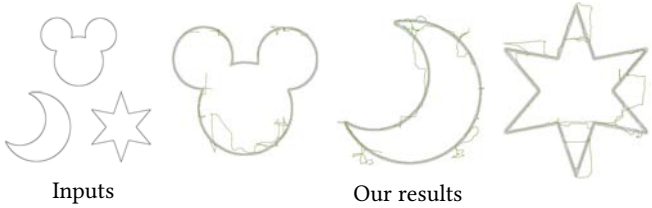

Fig. 18. **Limitations**. Our system fails to delineate clean contours with very simple shapes due to large inconsistency between input images.

wire sculpture is constructed, the user editing (Section 6) can run at interactive rate.

Optimization. While our results validate the capability of our algorithm for generating multi-view wire sculptures, the proposed method involves on several heuristic (and therefore brittle) optimization steps. Formulating the problem as a more principled global optimization framework is an important future direction.

Fabrication. Our system does not incorporate any physical simulations nor impose the single wire assumption as in [Liu et al. 2017]. Consequently, we cannot guarantee the generated wire sculptures are 3D printable. Possible ways to achieve fast and inexpensive 3D printing include considering the constraints of the wire-bending machine in the modeling process [Miguel et al. 2016], or decomposing the wire sculpture into a set of single wires and fabricating each wire separately.

8 CONCLUSIONS

We have presented a method for enabling novice users to construct multi-view wire sculptures. The core idea of our approach lies in reconstructing visual hull and extracting curve skeletons to balance projection error and spatial compactness. Through extensive evaluations in both simulation and 3D physical printout, we show that our method can produce smooth and compact wire sculptures exhibiting multiple prescribed images with minimum distortions. We believe that our framework can help democratize this unique art form and enable artists, designers, and hobbyists to create their own multi-view wire sculptures. We see several interesting future directions. This work focuses on creating wire sculptures with one connected component. Creating sculptures with multiple parts may provide more complex interactions among parts and offer richer viewing experiences. Our current approach resolves the inconsistency among input line drawings through minimizing the projection errors based on the original input images. An semantic-aware method may help significantly improve the visual quality by favoring projected lines that are plausible in the input line drawings.

ACKNOWLEDGMENTS

We are grateful to the anonymous reviewers for their comments and suggestions. We also like to thank National Applied Research Laboratories and Xian-Guang Zhong for helping on the 3D printing. The work is supported in part by the Ministry of Science and Technology of Taiwan (107-2218-E-007-047- and 107-2221-E-007-088-MY3).

REFERENCES

Marc Alexa and Wojciech Matusik. 2010. Reliefs as images. *ACM Trans. Graph. (Proc. of SIGGRAPH)* 29, 4 (2010), 60–1.

Amit Bermano, Ilya Baran, Marc Alexa, and Wojciech Matusk. 2012. Shadowpix: Multiple images from self shadowing. In *Comput. Graph. Forum (Proc. EUROGRAPHICS)*, Vol. 31. 593–602.

Robert T Collins. 1996. A space-sweep approach to true multi-image matching. In *Computer Vision and Pattern Recognition, 1996. Proceedings CVPR'96, 1996 IEEE Computer Society Conference on.* IEEE, 358–363.

Ricardo Fabbri and Benjamin Kimia. 2010. 3D curve sketch: Flexible curve-based stereo reconstruction and calibration. In *CVPR*.

Yasutaka Furukawa and Carlos Hernández. 2015. Multi-view stereo: A tutorial. *Foundations and Trends® in Computer Graphics and Vision* 9, 1-2 (2015), 1–148.

Yasutaka Furukawa and Jean Ponce. 2010. Accurate, dense, and robust multiview stereopsis. *IEEE Trans. Pattern Analysis Machine Intelligence* 32, 8 (2010), 1362–1376.

Michael Goesele, Noah Snavely, Brian Curless, Hugues Hoppe, and Steven M Seitz. 2007. Multi-view stereo for community photo collections. In *ICCV*.

Manuel Hofer, Michael Maurer, and Horst Bischof. 2017. Efficient 3D scene abstraction using line segments. *Computer Vision and Image Understanding* 157 (2017), 167–178.

Po-Han Huang, Kevin Matzen, Johannes Kopf, Narendra Ahuja, and Jia-Bin Huang. 2018. DeepMVS: Learning Multi-view Stereopsis. In *CVPR*.

Emmanuel Iarussi, Wilmot Li, and Adrien Bousseau. 2015. WrapIt: computer-assisted crafting of wire wrapped jewelry. *ACM Trans. Graph. (Proc. of SIGGRAPH Asia)* 34, 6 (2015), 221.

Jeroen Keiren, Freek van Walderveen, and Alexander Wolff. 2009. Constructability of trip-lets. In *25th European Workshop on Comp. Geom.*

Andreas Kuhn, Heiko Hirschmüller, Daniel Scharstein, and Helmut Mayer. 2017. A tv prior for high-quality scalable multi-view stereo reconstruction. *International Journal of Computer Vision* 124, 1 (2017), 2–17.

Ying-Miao Kuo, Hung-Kuo Chu, Ming-Te Chi, Ruen-Rone Lee, and Tong-Yee Lee. 2016. Generating Ambiguous Figure-Ground Images. *IEEE Trans. Vis. Comput. Graph.* PP (2016). Issue 99.

A. Laurentini. 1994. The Visual Hull Concept for Silhouette-Based Image Understanding. *IEEE Trans. Pattern Analysis Machine Intelligence* 16, 2 (1994), 150–162.

Svetlana Lazebnik, Yasutaka Furukawa, and Jean Ponce. 2007. Projective visual hulls. *International Journal of Computer Vision* 74, 2 (2007), 137–165.

Lingjie Liu, Duygu Ceylan, Cheng Lin, Wenping Wang, and Niloy J. Mitra. 2017. Image-based Reconstruction of Wire Art. *ACM Trans. Graph. (Proc. of SIGGRAPH)* 36, 4 (2017), 63:1–63:11.

L Liu, Erin W Chambers, David Letscher, and Tao Ju. 2010. A simple and robust thinning algorithm on cell complexes. In *Comput. Graph. Forum (Proc. EUROGRAPHICS)*, Vol. 29. 2253–2260.

Wojciech Matusik, Chris Buehler, Ramesh Raskar, Steven J Gortler, and Leonard McMillan. 2000. Image-based visual hulls. In *Proc. of ACM SIGGRAPH*.

Eder Miguel, Mathias Lepoutre, and Bernd Bickel. 2016. Computational Design of Stable Planar-rod Structures. *ACM Trans. Graph. (Proc. of SIGGRAPH)* 35, 4, Article 86 (2016), 11 pages.

Sehee Min, Jaedong Lee, Jungdam Won, and Jehee Lee. 2017. Soft shadow art. In *Proc. of the Symposium on Computational Aesthetics*. 3.

Niloy J. Mitra and Mark Pauly. 2009. Shadow Art. *ACM Trans. Graph. (Proc. of SIGGRAPH Asia)* 28, 5 (2009), 156:1–156:7.

Aude Oliva, Antonio Torralba, and Philippe G. Schyns. 2006. Hybrid Images. *ACM Trans. Graph. (Proc. of SIGGRAPH)* 25, 3 (2006), 527–532.

Luke Olsen, Faramarz F Samavati, Mario Costa Sousa, and Joaquim A Jorge. 2009. Sketch-based modeling: A survey. *Computers & Graphics* 33, 1 (2009), 85–103.

Jim Postell. 2012. *Furniture design.* John Wiley & Sons.

Alec Rivers, Frédo Durand, and Takeo Igarashi. 2010. 3D Modeling with Silhouettes. *ACM Trans. Graph. (Proc. of SIGGRAPH)* 29, 4, Article 109 (2010), 8 pages.

Johannes L Schonberger and Jan-Michael Frahm. 2016. Structure-from-motion revisited. In *CVPR*.

Johannes L Schönberger, Enliang Zheng, Jan-Michael Frahm, and Marc Pollefeys. 2016. Pixelwise view selection for unstructured multi-view stereo. In *ECCV*.

Wire Sculpture. 2007. https://en.wikipedia.org/wiki/Wire_sculpture. (2007).

Guy Sela and Gershon Elber. 2007. Generation of view dependent models using free form deformation. *The Visual Computer* 23, 3 (2007), 219–229.

Noah Snavely, Steven M Seitz, and Richard Szeliski. 2006. Photo tourism: exploring photo collections in 3D. In *ACM Trans. Graph. (Proc. of SIGGRAPH)*, Vol. 25. 835–846.

Richard Szeliski. 1993. Rapid octree construction from image sequences. *CVGIP: Image understanding* 58, 1 (1993), 23–32.

Anil Usumezbas, Ricardo Fabbri, and Benjamin B Kimia. 2016. From multiview image curves to 3D drawings. In *ECCV*.

WigJig. 2015. https://www.wigjig.com/. (2015).

Jungdam Won and Jehee Lee. 2016. Shadow theatre: discovering human motion from a sequence of silhouettes. *ACM Trans. Graph. (Proc. of SIGGRAPH)* 35, 4 (2016), 147.

Jonas Zehnder, Stelian Coros, and Bernhard Thomaszewski. 2016. Designing Structurally-sound Ornamental Curve Networks. *ACM Trans. Graph. (Proc. of SIGGRAPH)* 35, 4, Article 99 (2016), 10 pages.